ORIGINAL PAPER

Further examination of the criterion for crack initiation under mixed-mode I+III loading

K. H. Pham · K. Ravi-Chandar

Abstract   Mixed-mode fracture presents spectacular, scale-independent, pattern formation in nature and engineering applications. The criteria for crack initiation and growth under such mixed mode loading, however, are not well established. This work is aimed at exploring the failure criteria and the pattern formation under combined modes I and III. Specific designs of specimens based on boundary element simulations are considered with the aim of examining crack path selection at nucleation, threshold behavior of crack front fragmentation and, spacing of fragmentation. Experimental investigations with these specially designed geometries show that there *does not exist* a threshold ratio of $K_{III}^{\infty}/K_{I}^{\infty}$ below which a crack will propagate smoothly without fragmenting into facets. The crack front is shown to fragment immediately as soon as it is perturbed by a small amplitude mode III loading. The experimental results show further that spacing of the fragmentation is set not by any intrinsic length scale of the material, but by the characteristic dimension of the driving crack and the global loading.

K. H. Pham · K. Ravi-Chandar (✉)
Department of Aerospace Engineering and Engineering Mechanics, Center for Mechanics of Solids, Structures and Materials, The University of Texas at Austin, Austin, TX 78712-0235, USA
e-mail: ravi@utexas.edu

1 Introduction

The question of an appropriate criterion for fracture, although originally raised by Griffith nearly one century ago, is still being discussed, even within the restricted setting of linearly elastic materials, exhibiting a small-scale (nonlinear) fracture process zone. Griffith's criterion, as originally stated, is itself quite remarkable in its generality; subsequent attempts have only provided simplified implementations of this idea such as to permit applications to specific conditions of loading symmetries. For completeness, we quote the theory of rupture postulated by Griffith:

"…the problem of the rupture of elastic solids has been attacked from a new standpoint. According to the well-known 'theorem of minimum energy', the equilibrium state of an elastic solid body, deformed by specified surface forces, is such that the potential energy of the whole system is a minimum. The new criterion of rupture is obtained by adding to this theorem the statement that, the equilibrium position, if equilibrium is possible, must be one in which rupture of the solid has occurred, if the system can pass from the unbroken to the broken condition by a process involving a continuous decrease in potential energy. In

order, however, to apply this extended theorem to the problem of finding the breaking loads of real solids, it is necessary to take account of the increase in potential energy which occurs in the formation of new surfaces in the interior of such solids." …A.A. Griffith (1920).

In principle, this criterion should be able to predict arbitrary evolution of the crack(s), if such evolution is possible quasi-statically.[1] The total energy of the system is written as: $E = \Pi + U_s$ where U_s is the surface energy and $\Pi = -W_{\partial R} + U_R$ is the potential energy of the mechanical system. Griffith's postulated fracture criterion is then: $E'(a) = 0$ where a represents the equilibrium crack length. Griffith's example was a crack loaded with an opening mode symmetry with the consequence of a straight extension of the crack and he equated the fracture energy to the surface energy (surface tension), but the theory itself corresponds to the standard idea of energy minimization, and has no such restrictions. In principle, when considering $E'(a) = 0$, all possible crack configurations must be considered, and all possible source of dissipation that occur prior to generation of failure could be introduced into U_s, not just the surface energy. Therefore, the criterion for selection of the crack path (or nucleation of a crack) is embedded in Griffith's postulate; the main hurdle is that it is extremely difficult to extract the path corresponding to this minimization unless special methods are introduced to permit crack surface evolution! The change in the mechanical potential energy (outside of the crack surface energy) $-d\Pi/da = G$ is labeled the elastic energy release rate.

Practical fracture *criteria* (note plural) have been introduced since the time of Irwin (1957), that, while still based on the Griffith theory, are of limited validity. Nevertheless, such criteria are of enormous practical significance since they permit the design of fracture critical structures, determination of residual strength of structural components in the presence of cracks, and assessment of structural integrity in a large number of applications. The separation of the global loading into the three symmetries—opening mode (mode I), in-plane shearing mode (mode II) and anti-plane shear mode (mode III)—is an extremely useful exercise that decouples the problem of crack path selection from

the energy balance equation, at least for mode I. Since mode I loading is perhaps the most prevalent in structural applications, such decoupling has permitted successful development of a practical fracture theory.

For mode I, based on the Williams (1952) and Irwin (1957) estimate of the singular crack tip stress field, $\sigma_{\alpha\beta} = K_I^\infty (2\pi r)^{-1/2} f_{\alpha\beta}(\theta)$, where K_I^∞ is the mode I stress intensity factor (SIF), and $f_{\alpha\beta}^I(\theta)$ is a known angular distribution, the connection to the Griffith criterion can be written as $G = (1-\nu^2)(K_I^\infty)^2/E$. The Griffith fracture criterion can be written as $K_I^\infty = K_{IC}$ at onset of crack growth, where K_{IC} is the *fracture toughness* and is related to the *fracture energy per unit area* G_c by $\sqrt{EG_c} \equiv K_{IC}$. This should be considered to be a solved problem, apart from the search for numerical methods that can implement this in a robust calculation.

For problems involving coupled in-plane modes I+II, the stress field in the vicinity of the crack tip is written as: $\sigma_{\alpha\beta} = K_I^\infty (2\pi r)^{-1/2} f_{\alpha\beta}^I(\theta) + K_{II}^\infty (2\pi r)^{-1/2} f_{\alpha\beta}^{II}(\theta)$, where K_{II}^∞ is the mode II stress intensity factor, $f_{\alpha\beta}^{II}(\theta)$ is another known angular distribution, and the connection to the Griffith criterion can be written *formally* as: $G = (1-\nu^2)\left((K_I^\infty)^2 + (K_{II}^\infty)^2\right)/E$. However, it must be noted that this estimate of the energy release rate is strictly valid only for a straight line extension of the crack; however, it is expected that due to the asymmetry in the loading under combined modes I+II, that the crack will in general experience a curved or kinked crack evolution, depending on the magnitude of the asymmetry that is dictated by the ratio: K_{II}^∞/K_I^∞. At least three different formulations of the failure criterion have been used in the literature: (i) Griffith—crack grows in the direction of the maximum energy release, when this attains the fracture energy, G_c. Calculation and implementation of this criterion has been difficult and awaits the development of numerical or other methods—such as the phase field method—for determining this path. (ii) Maximum hoop stress criterion—crack grows in the direction perpendicular to which the hoop stress reaches a maximum; of course, the energy released in this direction will be a function of the stress intensity factors; therefore, this criterion can be written as: $F(K_I^\infty, K_{II}^\infty) = 0$. (iii) Principle of local symmetry (PLS): consider an infinitesimal extension of the main crack along some direction, γ, and denote the

---

[1] If dynamic fracture is to be considered, inclusion of kinetic energy is essential.

stress intensity factors at the tip of such extension as $(k_I(\gamma), k_{II}(\gamma))$; the crack will grow in the direction γ_c in which the local mode II stress intensity factor vanishes: $k_{II}(\gamma_c) = 0$, when $k_I(\gamma_c) = K_{IC}$. The scatter in the available experimental data prevents a positive discrimination between the predictions of the maximum hoop stress criterion and the principle of local symmetry; within these limits, both the PLS and the maximum hoop-stress criterion appear to provide acceptable predictions of crack path and growth. Combined modes I+II also represents a nearly solved problem; additional investigations could be fruitful if directed towards design of suitable experiments that could discriminate between the different failure criteria and towards development of robust numerical methods for implementation of these failure criteria.

For problems involving mixed modes I+III, the situation is much less developed for many different reasons. First, there have been limited attempts, some experimental and others analytical, to extract/elucidate the appropriate failure criterion. Second, the available experimental investigations have been clouded somewhat by uncertainties associated with the actual loading/boundary conditions that bring to question the mode mix really responsible for crack initiation/growth. Lastly, while the anti-plane shear problem for deformation is governed by Laplace's equation in two-dimensions, the corresponding fracture problem must include additional specification of the nature of the failure process before the need for three-dimensional analysis can be determined; thus, on the one hand, if failure is taken to be caused by slip along planes of maximum shear (as in the work of Barenblatt and Cherepanov 1961), the mode III problem remains two-dimensional, and such "shear cracks" can propagate with the normal to the crack surface remaining in the plane and maintaining the anti-plane symmetry. In fact, in this case, the mode III problem is fully decoupled from the in-plane modes I+II. Barenblatt and Cherepanov (1961) used this criterion to solve a number of different crack problem in pure mode III. On the other hand, if one considers that failure is caused by opening stresses, one *must abandon the assumption that the solutions retain antiplane symmetry*; the fracture problem is then inherently three dimensional, and indicates possibly discontinuous evolution of the crack that make analysis difficult. This distinction has not always been maintained clearly in the literature, with most analyses of
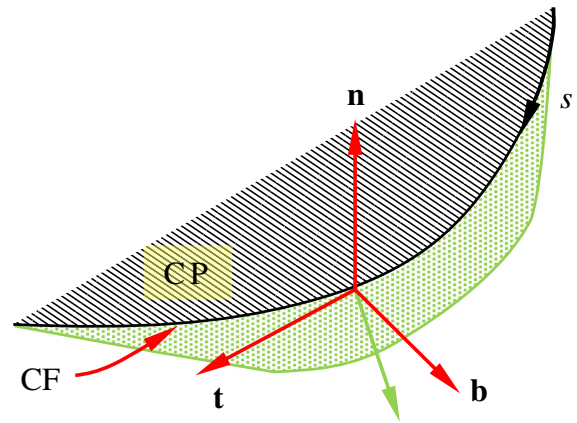

Fig. 1 Schematic diagram of a three dimensional crack front. *CF* and *CP* represent the crack front and crack plane, respectively. $(\mathbf{b}, \mathbf{n}, \mathbf{t})$ represent the directions normal to *CF*, normal to *CP*, and tangent to the *CF* respectively

the problem implicitly assuming failure by opening stresses.

One generalization of the PLS was proposed by Goldstein and Salganik (1974) is the following postulate: $k_{II}(\gamma_c) = 0$, with $f(k_I, k_{III}) = 0$; here k_{III} represents the mode III SIF at the extension of the main crack along the orientation γ_c. As with the criterion posed by Barenblatt and Cherepanov (1961), this is a possible criterion and its implications must be evaluated for specific mixed mode loading conditions to determine its suitability. In order to explore the predictions of this criterion, we use the perturbation estimates of Leblond (1999) to express the fracture criterion in terms of the SIF on the original crack faces. Consider a local region of a curved crack front (CF), with the position along the crack indicated by the arc length s as shown in Fig. 1. The unit vector $\mathbf{t}(s)$ is tangent to the CF, the unit vector $\mathbf{n}(s)$ is normal to the original crack plane (CP) and the unit vector $\mathbf{b}(s)$ indicates the normal to the CF and completes the triad of unit vectors at the point s. The cracked solid is subjected to arbitrary loading such that the crack tip experiences a combined mode I+II+III loading indicated by $\left(K_I^\infty(s), K_{II}^\infty(s), K_{III}^\infty(s)\right)$ along the $(\mathbf{n}(s), \mathbf{b}(s), \mathbf{t}(s))$ directions, respectively. Leblond (1999) established that for a perturbation of the crack that evolves continuously from the original crack font, that $k_p(\gamma) = F_{p,i} K_i^\infty$, where p and i take the values I,II,III, (summation over repeated index is implied, but the comma is used simply to separate the two sub-

scripts) and γ is the tilt angle with respect to the $\mathbf{t}(s)$ axis. Using symmetry arguments Leblond (1999) suggests that $F_{i,p} = 0$ when either p or i takes the value III; this results in a complete decoupling of the in-plane ($\mathbf{b} \times \mathbf{n}$) loading modes from the anti-plane modes.[2] The consequences of this decoupling are examined in the following; the fracture criterion according to the PLS can now be written as

$$k_{II}(\gamma) = F_{II,I}(\gamma) K_I^\infty + F_{II,II}(\gamma) K_{II}^\infty = 0$$
$$k_{III}(\gamma) = F_{III,III}(\gamma) K_{III}^\infty$$
$$f \left[F_{I,I} K_I^\infty + F_{I,II} K_{II}^\infty, F_{II,I} K_I^\infty \right.$$
$$\left. + F_{II,II} K_{II}^\infty, F_{III,III} K_{III}^\infty \right] = 0 \qquad (1)$$

The first equation above dictates the direction of crack extension γ_c: setting $k_{II}(\gamma_c) = 0$ yield indicates that the direction of crack extension is influenced only by the ratio of $K_{II}^\infty(s)/K_I^\infty(s)$, the second equation provides the value of $k_{III}(\gamma)$, while the third is the energy balance equation; note that $K_{III}^\infty(s)$ contributes only to the energy released or equivalently the crack initiation load level, but does not influence the crack path. This situation is clearly of limited validity: for example, consider a half-plane crack with a straight crack front subjected to a constant initial SIF: $\left(K_I^\infty(s) = a, K_{II}^\infty(s) = b, K_{III}^\infty(s) = c \right)$. The PLS criterion suggests that the angle γ_c is dictated only by the ratio b/a and is completely independent of c. If we take $b = 0$, thereby considering a pure mode I crack, the PLS failure criterion as postulated above predicts crack extension along $\gamma_c = 0$ for all values of c. Experiments, going all the way back to Smekal (1953) have shown that even a small magnitude of c in a dominant mode I problem will nucleate new crack fragments along the CF that are inclined at an angle so as to eliminate k_{III}. The insistence on continuous evolution of the crack that is inherent in this criterion makes it applicable only when K_{III}^∞ is small; this raises one fundamental question of *whether there exists a threshold ratio $K_{III}^\infty/K_I^\infty$ below which continuous extension of the crack may occur*. Such a threshold will place a limit on the applicability of the PLS criterion.

Since we know that mode III loading is important in crack front evolution, we seek a different generalization of the PLS: if in-plane cracks evolve so as to

eliminate shear, the natural generalization would be to insist that 3D cracks also evolve so as to eliminate shear. Based on the experiments of Sommer (1969), Knauss (1970), Cooke and Pollard (1996), and Lin et al. (2010), we revisit the criterion that eliminates all shear induced SIF and postulate that the crack will propagate along the direction (γ_c, ϕ_c) when $k_I(\gamma_c, \phi_c) = K_{IC}$, $k_{II}(\gamma_c, \phi_c) = 0$, $k_{III}(\gamma_c, \phi_c) = 0$. A simple interpretation of this criterion is that the first provides the condition of criticality, while the second and third dictate the rotation angle γ_c of the crack normal about the $\mathbf{t}(s)$ and angle ϕ_c about the $\mathbf{b}(s)$ axes—the tilt and twist, respectively. However, crack twisting cannot be achieved by a continuous evolution of the crack front; this requires the crack front to fragment—through the generation of crack nuclei—immediately upon application of a nonzero K_{III}. This raises the second fundamental question: *what, if any, sets the intrinsic scale for the spacing between the nucleated crack front fragments.* Since linear elastic fracture theory does not provide an intrinsic length scale, this length must arise from other geometrical features of the problem—either an intrinsic process zone or a macroscopic length scale.

The focus of this article is on the initiation of mode I+III cracks, addressing the two fundamental questions raised above. We examine the initiation of mixed mode I+III cracks through a systematic variation of specimen design that enables addressing the issue of the existence of a threshold as well as an intrinsic length scale for the fragmentation of the crack front. This article is organized as follows: recent work on mixed-mode I+III cracks is reviewed in Sect. 2. The design of specimens aimed at revealing the underlying reasons for crack front fragmentation are discussed in Sect. 3. The results are discussed in Sect. 4, with particular attention to the question of the existence of a threshold for the occurrence of fragmentation along the crack front, and the question of pattern formation from the resulting crack initiation. The main outcomes and their implication on fracture modeling are summarized in Sect. 5.

2 Background for the mode I+III problem

We assume that fragmentation of the crack front into facets of new cracks is an important aspect of mixed mode I+III crack initiation and address two main ques-

---

[2] It should be noted that the coupling between the in-plane and anti-plane modes occurs in case of helicoidal perturbation (see Leblond et al. 2011).

tions: (i) is there a threshold level of K_{III}^∞, below which continuous evolution of the crack front is possible, and (ii) what sets the length scale of fragmentation? The relevant literature is reviewed in this section.

It has long been postulated that the crack will propagate in a direction perpendicular to the maximum principal stress (see Sommer 1969; Knauss 1970); under this criterion, the orientation for conditions of plane strain is given by Cooke and Pollard (1996):

$$\left(\frac{1}{2} - \nu\right) \tan(2\phi_c) = \frac{K_{III}^\infty}{K_I^\infty} \qquad (2)$$

Experimental observations support the above postulate for crack initiation (see Knauss 1970; Yates and Miller 1989; Cooke and Pollard 1996; Lazarus et al. 2008; Lin et al. 2010); in particular, the pure mode III experiment of Knauss (1970) indicates an angle of the cracks to be $\pi/4$ in agreement with the prediction of Eq. (2). Cooke and Pollard (1996) showed that this criterion is equivalent to $k_{III} = 0$ and maximum k_I criterion; both these criteria indicate that $\phi_c \rightarrow \pi/4$ as $K_{III}^\infty/K_I^\infty \rightarrow \infty$. Cooke and Pollard (1996) also considered the maximum energy release rate criterion; this was evaluated by a simple perturbation analysis where the SIFs on the twisted cracks were obtained by imposing the stress from the parent crack; for values of $K_{III}^\infty/K_I^\infty > 1.4$ (for $\nu = 0.38$), the predictions of this criterion deviated from that of the maximum principal stress criterion with two branches, tending towards $\phi_c \rightarrow 0$ or $\phi_c \rightarrow \pi/2$ as $K_{III}^\infty/K_I^\infty \rightarrow \infty$. Clearly, the pure mode III results of Knauss (1970) indicate that $\phi_c \rightarrow \pi/4$ as $K_{III}^\infty/K_I^\infty \rightarrow \infty$ and contradict the predictions based on energy release. Nevertheless, one cannot discard the maximum energy release rate criterion since it is obtained from a fundamental principle; it would appear that the perturbation estimate for the energy release rate requires additional investigation. In the following, we shall assume that the crack will develop fragments in agreement with the orientation predicted by the maximum principal stress criterion in Eq. (2).

Sommer (1969) examined the role of superposed mode III loading on a crack growing under a dominant mode I loading. The lateral surface of a cylindrical glass rod was subjected to fluid pressure; the fluid penetrated to the inside through surface flaws and then generated an opening mode interior crack perpendicular to the axis of the rod. By superposing a small torque on the rod, the fluid pressure driven crack was then subjected to a small additional mode III loading. In this case, Sommer observed a transition from a smooth to faceted fracture surface; such a transition had been observed earlier by Smekal (1953), who called the fragments "fracture lances" and associated this transition with the competition of mode III and mode I. In Sommer's experiments, mode III is negligibly small when the crack is in the central portion of the rod but increases as it grows towards the outer surface. The experiments were performed at three levels of torsion and the radius and crack tilt angle at the location of the initiation of faceted cracks were measured. Based on the experimental data, Sommer postulated that for lance initiation (fragmentation), a minimum angle of twist of the principal axis was necessary. This minimum angle is presumably dictated by intrinsic material properties and was measured to be $3.3°$ with respect to the nominal crack plane for the AR-glass tested. The existence of the minimum twist angle of the crack is equivalent to a threshold ratio $K_{III}^\infty/K_I^\infty$ above which the crack front will fragment into facets and below which the crack surface will exhibit smooth undulations.

Recently, Pons and Karma (2010) studied the instability of helical crack-fronts under mixed mode loading using a continuous phase-field method that permitted the evolution of the crack front to be examined. In their notation, the ($\mathbf{b}$, $\mathbf{n}$, $\mathbf{t}$) directions at a local point on the CF are denoted as (x, y, z). Mixed mode I+III loading was imposed by choosing the initial opening and out-of-plane sliding displacements in y and z directions, respectively. The crack front was perturbed helicoidally; the perturbation amplitude also changes exponentially in time (or crack extension along x) and was parameterized in the form:

$$\delta x_{front}(z, t) + i\delta y_{front}(z, t)$$
$$= A_0 \exp\left[-ikz + \frac{\sigma(k)t}{\tau}\right] \qquad (3)$$

Based on this parameterization, the variation of the perturbation amplitude versus time for simulations with different wave number k and $K_{III}^\infty/K_I^\infty$ were obtained and used to extract the linear stability spectrum $\sigma(k)$. The simulated data was fitted to the form $\sigma(k) = ak - bk^2$. The spectrum is characterized by the fastest-growing wavelength $\Lambda_{max} = 2\pi/k_{max}$, where $\sigma(k_{max})$ reaches the peak value, and the marginally stable wavelength $\Lambda_{stable} = 2\pi/k_{stable}$, where $\sigma(k_{stable})$ van-

ishes and $\Lambda_{\max} \approx 2\Lambda_{stable}$. Then a relation between Λ_{stable} and $K_{III}^\infty / K_I^\infty$ and a "process zone" length scale ξ was developed by equating the configurational force with the cohesive force and imposing the maximum fracture energy release rate criterion. This yields an approximate relation for the maximally unstable wavelength:

$$\Lambda_{\max} \approx 2\Lambda_{stable} \approx 4\pi\xi \left(\frac{K_I^\infty}{K_{III}^\infty} \right) \quad (4)$$

Based on this result, the authors postulated that the initial instability wavelength depends solely on the stress intensity factors for modes I+III and the process zone scale. It should be noted that a threshold behavior is not predicted by this analysis; for each loading condition, $K_{III}^\infty / K_I^\infty$, there exists a critical wavelength of fragmentation. Following on this numerical effort, Leblond et al. (2011) derived an analytical expression of the variation of the SIF near a helicoidally perturbed crack front using the results of Movchan et al. (1998). They used this expression in linear stability analysis and identified that helicoidal perturbations are unstable beyond a critical ratio of $K_{III}^\infty / K_I^\infty$ that depends on the Poisson's ratio:

$$\left(\frac{K_{III}^\infty}{K_I^\infty} \right)_{cr} = \sqrt{ \frac{(1-\nu)(2-3\nu)}{3(2-\nu) - 4\sqrt{2}(1-2\nu)} } \quad (5)$$

For a Poisson's ratio of $\nu = 0.22$ and $\nu = 0.34$, corresponding to glass and Homalite-100,[3] respectively, the critical values are 0.69 and 0.45. However, Sommer's experimental results indicate that fragmentation occurs when the ratio $K_{III}^\infty / K_I^\infty \sim 0.03$; this observation suggests that there is possibly another mode of instability that intervenes prior to reaching the helocoidal instability with a continuous evolution of the crack front.

Lin et al. (2010) suggested a generalization of the PLS criterion. They impose that both local shear SIFs vanish on the incipient crack, and that the local opening mode SIF approaches the critical value for the material:

$$k_I = K_{IC}, \; k_{II} = 0, \; k_{III} = 0, \quad (6)$$

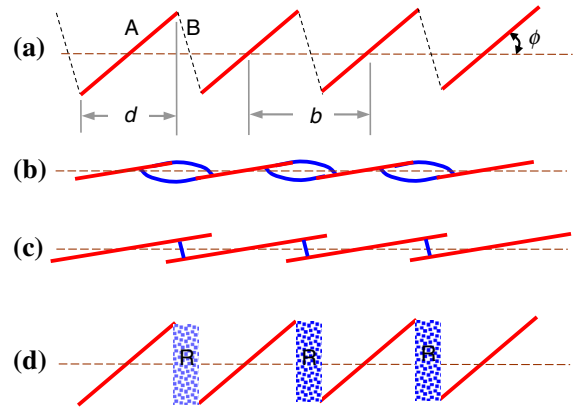[3] Homalite-100 (abbreviated as H-100) is a brittle thermosetting polymer commonly used in fracture studies.

Fig. 2 a Geometry of the "factory roof" profile in a plane perpendicular to the crack propagation direction; the *red lines* indicate type A cracks inclined at an angle ϕ with respect to the nominal crack plane and the black dashed lines indicate type B cracks; **b** "Hand-shaking" mode of linking of the type A cracks; **c** Bridging cracks linking type A cracks, formed after rearrangement of the stress field; **d** Representation of bringing regions R that connect the type A cracks and provide energy penalty for the overall extension of the crack. (reproduced from Lin et al. 2010)

This criterion requires the crack front to fragment into new faceted cracks as soon as a small amount of mode III loading is applied. The plane of the prospective crack (twist angle ϕ_c) is dictated by the Eq. (2). The cross-section perpendicular to the original crack surface exhibits a "factory roof" profile (see Fig. 2). There are two types of cracks corresponding to the two twist angles in this factory-roof pattern: cracks of type A (*en echelon cracks*) are formed by opening mode I, and cracks of type B which are not favorably oriented with respect to local opening mode I. Therefore, type B cracks cannot form concurrently with the type A cracks. Based on experimental observation of the dynamic crack growth, Lin et al. (2010) proposed that type A cracks form first, but the region between them (*bridging region*) is either uncracked or breaks later. The energy penalty associated with the bridging region must be paid as the type A cracks develop. By balancing the local energy dissipation per unit crack extension with the global dissipation, Lin et al. (2010) developed a relationship between the twist angle and the space of new crack fronts:

$$\Gamma d \sec \phi_c + \gamma_s \alpha d \tan \phi_c = \tilde{\Gamma} \left(\frac{K_I^\infty}{K_{III}^\infty} \right) b \quad (7)$$

Fig. 3 a The specimen
configurations used by
Goldstein–Osipenko **b**
schematic representation of
sections of the specimen at
different distances from the
notch and **c** images of
similar sections from the
notch on cheese specimens
indicating (i) the absence of
type *B* cracks and (ii) the
coarsening of the fractures
(reproduced with
permission from Goldstein
and Osipenko 2012)
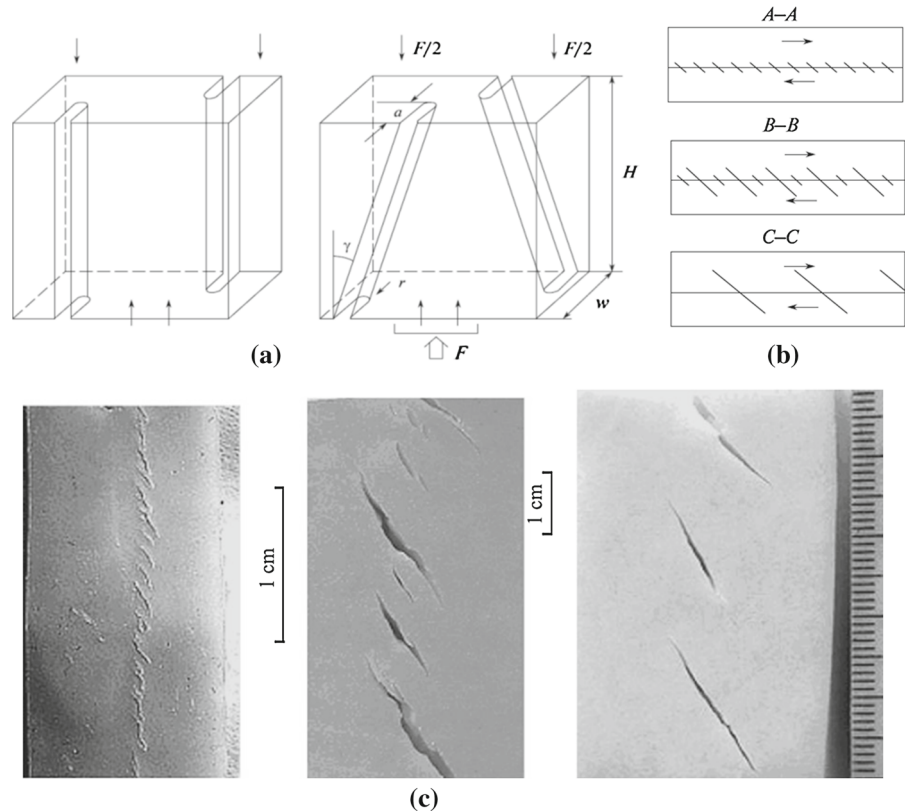
where b, d and ϕ_c are defined in Fig. 2. Γ is the energy
penalty per unit area for type *A* cracks. $\tilde{\Gamma}$ is the global
fracture energy corresponding to the appropriate ratio
of $K_{III}^\infty / K_I^\infty$. γ_s, α are the energy penalty per unit vol-
ume and the characteristic width associated with the
bridging region. Based on Eq. (7), they postulated that
there exists an intrinsic length scale b (the scale of non-
locality) which is set by material properties. Experi-
mental data on d and twist angle ϕ_c of the fracture
surface from three point bending specimens with slant
crack at the center was collected. Fitting the data to the
model, they were able to extract the scale of nonlocality
b and the energy penalty associated with the bridging
region γ_s.

Recently, Goldstein and Osipenko (2012) examined
this problem by performing and interpreting experi-
ments on gypsum and cheese; their specimen, shown
in Fig. 3, experiences dominant mode I, with a super-
posed mode III loading. They calculated the stress
intensity factor at the fragmented crack approximately
and explored the reasons for the coarsening of the
crack fragments; we will examine this configuration
in greater detail in this work. An important outcome

of their work is the demonstration (see Fig. 3) that
type *B* cracks are not formed at the same time as the
type *A* cracks. Coarsening of the spacing between the
fragmented cracks was also observed, but we will not
consider this aspect in the present work. Lazarus et al.
(2008) had examined this issue earlier in PMMA spec-
imens subjected to fatigue cyclic loading and demon-
strated the absence of type *B*.

3 Specimen design

As discussed above, different specimen geometry and
loading configurations have been explored in the liter-
ature in order to elucidate initiation and growth of frac-
ture under mixed mode I+III conditions. However, con-
trolling the exact combination of mixed mode loading
is quite difficult; in particular, while the primary interest
is in the combination of modes I+III, it is extremely dif-
ficult to eliminate mode II loading, except in some spe-
cial cases, such as the internal pressure combined with
superposed torsion. In the present work, we begin with
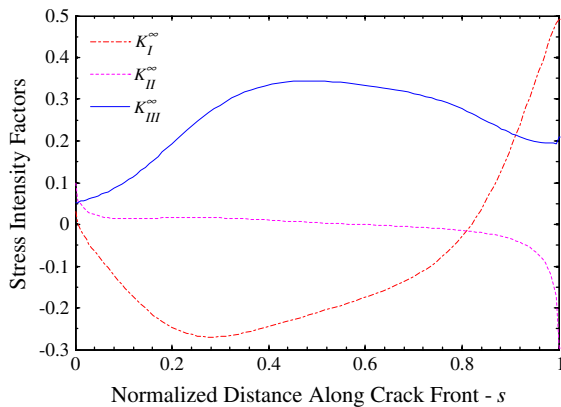the geometry and loading considered by Goldstein and

Fig. 4 The variation of the stress intensity factors $K_I^\infty(s)$, $K_{II}^\infty(s)$, $K_{III}^\infty(s)$ along the crack front in the Goldstein–Osipenko configuration with slant cracks with $\gamma = 15°$

Osipenko (2012) shown in Fig. 3. Then, we consider modifications to this geometry and loading in order to control the crack tip state; specific designs of specimens were based on accurate calculations of the stress intensity variations using a boundary element technique, and are aimed at examining crack path selection at nucleation, threshold behavior of crack front fragmentation, and the spacing of fragmentation. Using these variants of the Goldstein–Osipenko geometry, we are able to expand the range of $K_{III}^\infty/K_I^\infty$ that can be examined.

3.1 Goldstein–Opisenko geometry and variants

We performed a number of simulations to calculate the SIFs using a Symmetric Galerkin Boundary Element code (Li and Mear 1998; Li et al. 1998). First, the Goldstein–Osipenko geometry shown in Fig. 3 was simulated with the following dimensions: $H = 2.0$, $w = 1.0$, $\gamma = 15°$ and $a = 0.25w$. The variation of the mode I, II and III SIFs for this geometry along one of the cracks is shown in Fig. 4;[4] it is clear that the mode I SIF is negative, indicating crack closure/contact for sharp cracks, and that the mode III SIF reaches very large values. We note that the simulations considered an ideally sharp crack, while the experimental crack would have some bluntness arising from the fabrication process. At the central portions of the crack front,

---

[4] In this and other plots showing the stress intensity factor variation, the curvilinear coordinate normalized by the total crack front length along the pre-crack front is used as the normalized crack front position s.

this combined mode I+III SIF will cause crack initiation with an angle ϕ_c with respect to the main crack plane and possibly trigger crack front fragmentation. However, in addition to these two modes, it can be identified readily that the mode II SIF is singular at the surface where the crack intersects the free surface and varies monotonically across the specimen. Such variation of K_{II}^∞ was pointed out by Lin et al. (2010) for the bending specimen. The role of this K_{II}^∞ is to kink the crack to attain local mode I conditions; in brittle materials such as glass and H-100, the effect of mode II is very strong and causes the crack to follow a tortuous surface under all three modes. Therefore, we sought a modification to the Goldstein–Osipenko geometry that would eliminate the mode II SIF.

3.2 Calculation of stress intensity factors

In the second set of simulations, the geometry was modified with a design of a part-through crack as shown in Fig. 5; for the loading configurations considered, the part through crack is not expected to generate a mode II stress intensity factor at the point where the crack meets a free surface. Two interesting specimen types were found, Type I that introduces predominantly mode I+III loading, while Type II generates negative mode I along most of the pre-crack front.

Specimen Type I: The geometry is shown in Fig. 5a. The specimen is loaded from the top and supported at the bottom of two pre-cracks. The specific dimensions used are as follows: $L = 3.0$, $H = 2.0$, $d = 2.25$, $a = 0.186$, $b = 0.2$, $r = 1.5$, $\gamma = 26.6°$, and $D = 0.5$ for H-100 and $D = 0.75$ for glass. The variation of the stress intensity factors for all three modes along the curved crack front are shown in Fig. 6. There exist some interesting characteristics to the variation of the SIFs along the crack front that are useful in mixed-mode I+III investigations. K_I^∞ is positive and dominates the loading with a very large amplitude. K_{II}^∞ is very small in the central regions of the CF $0.4s - 1.0s$; it should also be noted that, as expected, it goes to zero at $s = 0$ and $s = 1$, where the crack pierces to the free surface. K_{III}^∞ is large over some portion of the crack front, but only in locations where K_I^∞ is small. The most interesting part is that K_{III}^∞ switches sign along the pre-crack front; at $s = 0.82$ K_I^∞ reaches the maximum value, and both K_{II}^∞ and K_{III}^∞ nearly vanish; (we will refer to this location as the *transition point*). The

Fig. 5 Geometry of
modified
Goldstein–Opisenko
configurations. The crack
fronts are curved and break
the surface on planes
$y = \pm D/2$. Specimen Type
II is obtained merely by
flipping the loading about
the xy-plane. **a** Specimen
Type I. **b** Specimen Type II.
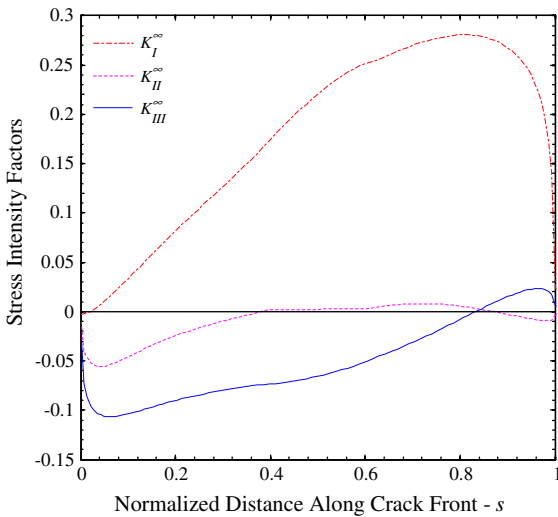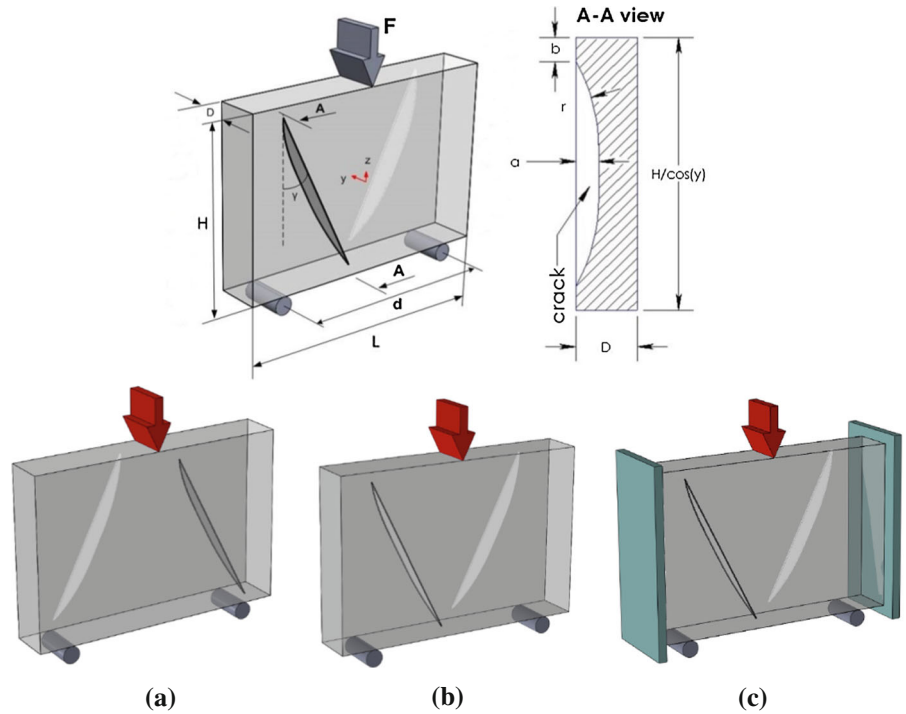**c** Specimen Type III

Fig. 6 The variation of the stress intensity factors
$K_I^\infty(s), K_{II}^\infty(s), K_{III}^\infty(s)$ along the crack front for speci-
men type I. The origin of s is located at the *top* of the specimen.
Elastic properties of glass have been assumed in the simulations.
The specimen redesign has eliminated the concentration of
mode II stress intensity factor where the crack meets a free
surface ($\gamma = 26°$)

importance of this specimen design is that it can pro-
vide a critical test to the existence of a threshold for
the fragmentation of the crack front. First, according to

the criterion postulated by Lin et al. (2010), we expect
the initiation of crack growth to occur at the transition
point, where K_I^∞ approaches the critical value K_{IC},
while K_{II}^∞ and K_{III}^∞ both vanish; the principle of local
symmetry would also suggest crack initiation at this
location. Based on Eq. (2), we would also expect to see
the twist angle on either side of the transition point to
be of opposite signs. However, if there exists a thresh-
old ratio of $K_{III}^\infty/K_I^\infty$ where the fragmentation does
not occur, we should observe a continuous evolution of
the crack front without fragmentation in region around
the transition point. The extent of this region can be
estimated from the Sommer's results (Sommer 1969);
if a minimum twist angle of 3.3° is necessary for frag-
mentation to occur in glass, based on Eq. (2), this yields
a threshold ratio of $K_{III}^\infty/K_I^\infty$ equal to 0.029 for glass
assuming $\nu = 0.25$. From the simulation result for the
SIFs, one should observe a flat portion of normalized
length 0.042 (equivalent to 2.044 mm for the speci-
men dimensions indicated earlier) around the transi-
tion point. We will address this through experiments
on glass and H-100.

Specimen Type II: Specimen Type I has a very large
mode I stress intensity factor. As a result, when crack
initiation occurs (particularly in the somewhat blunted
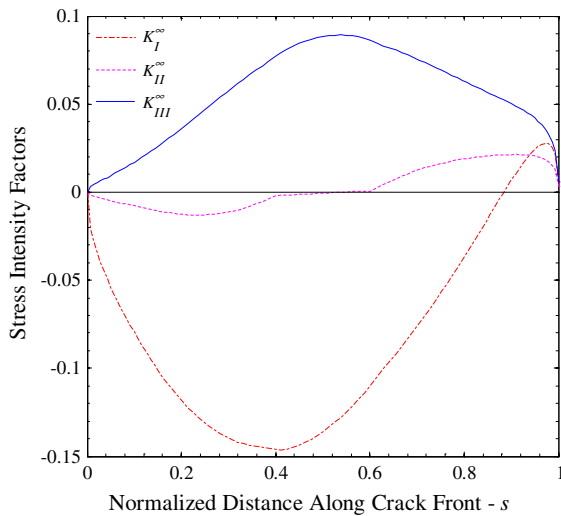specimens that were manufactured), further growth is

Fig. 7 The variation of the stress intensity factors $K_I^\infty(s)$, $K_{II}^\infty(s)$, $K_{III}^\infty(s)$ along the crack front for specimen type II. The origin of s is located at the *top* of the specimen. Elastic properties of Homalite-100 have been assumed in the simulations ($\gamma = 26°$)

Fig. 8 The variation of the stress intensity factors $K_I^\infty(s)$, $K_{II}^\infty(s)$, $K_{III}^\infty(s)$ along the crack front for specimen type III. The origin of s is located at the *top* of the specimen. Elastic properties of Homalite-100 have been assumed in the simulations ($\gamma = 26°$)

extremely dynamic and interpretation of the fracture surface beyond the onset of crack initiation becomes quite difficult. In an effort to modify the stability of crack growth in the specimen, we flipped the orientation of the specimen with respect to the loading direction for specimen Type I as shown in Fig. 5b, making it close to the Goldstein–Osipenko specimen geometry, with the exception of the curved crack fronts. The variation of the three stress intensity factors along the crack front is shown in Fig. 7. In contrast to the Type I specimen, K_I^∞ is negative over most of the crack front except for the portion close to the bottom of the specimen; the largest compressive values of K_I^∞ occur in the same region where K_{III}^∞ is also large; $K_{II}^\infty \sim 0$ in this segment, indicating that we have a segment over which crack initiation will be governed by K_{III}^∞ and K_I^∞, but with tilt angles that are opposite to that expected in Type I specimens. The nucleation should occur first in the central regions and the cracks may grow in a stable manner until nucleation occurs in the region of positive K_I^∞.

Other variants of the Goldstein–Osipenko geometry were considered; for example, in order to prevent the possible nucleation of cracks from the positive K_I^∞ in specimen Type II, a compressive stress was applied on the two vertical surfaces as indicated in Fig. 5c; The resulting variation of the three stress intensity factors is
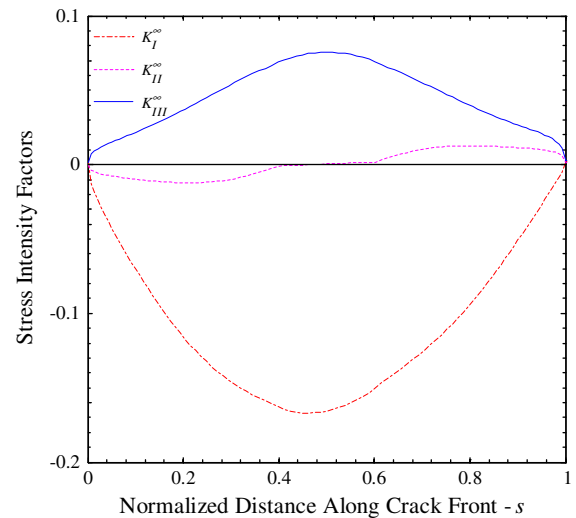
shown in Fig. 8. This geometry provides a nice symmetry in the loading; compressive , nearly negligible K_{II}^∞, and a large K_{III}^∞ are observed. However, the large compression in the vicinity of the maximum shear makes it difficult to initiate crack growth in this geometry. Preliminary experiments indicated that prior to crack initiation from the machined crack tips, cracks nucleated from other defects near the free surfaces of the specimen under mode I conditions and grew dynamically. Tabulated values of the stress intensity factor variation for the Goldstein–Osipenko geometry and its three variants considered here are given in the "Appendix".

4 Experimental results

Parallelopipedic specimens 50.8×76.2 mm (2×3 in; height × length;) were machined from 12.7 mm (0.5 in) thick H-100 and 19 mm (0.75 in) thick glass sheets. The cracks were cut according to the specimen design of types I and II, using a diamond blade with radius 38.1 mm (1.5 in) and thickness 0.178 mm (0.007 in). Although an extremely thin diamond blade was used to machine the crack, the pre-crack front is far from the idealized sharp crack front. There also exist many groove lines along the blunt pre-crack front that are caused by the hard particles that form the diamond-

Fig. 9 Fractograph of Homalite H-100 specimen type I, showing the region near the transition point. **b** Shows a magnification of the boxed region in **a**
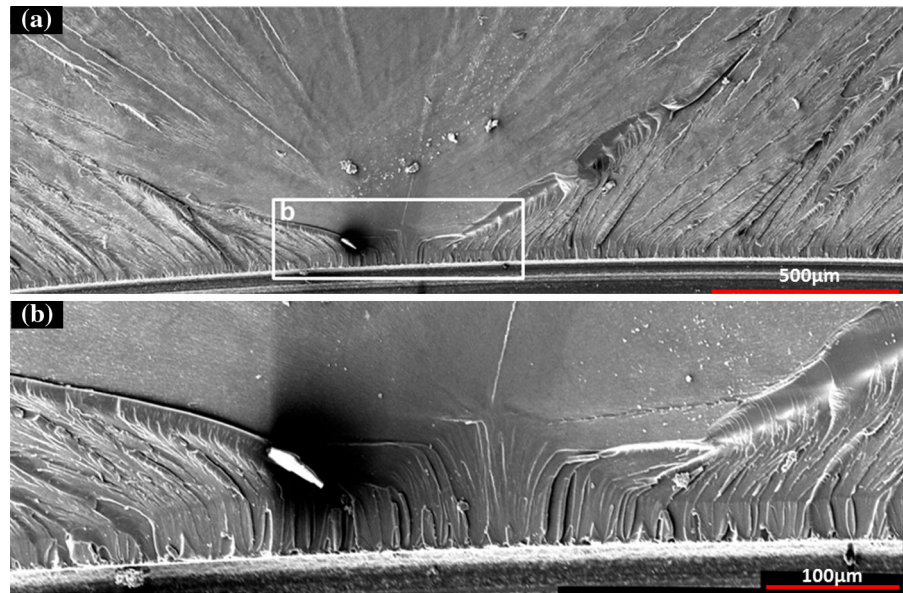

coated cutting blade. The experiments were performed under displacement control in an Instron Model 4482 testing machine. The load vs load-point displacement was monitored. However, in all the tests performed, the response was linear until abrupt and unstable fracture initiation. The critical load varied significantly from test to test due to the fact that there were variations in crack tip state; however, the geometric aspects of the response were repeatable to permit interpretation of the threshold behavior, fragment spacing etc.

4.1 Threshold behavior

The main objective of the tests performed with specimen of Type I was to examine the response of the crack when K_{III}^{∞} passes through zero. Therefore, the fracture surface of the glass and H-100 specimens of Type I were examined using a scanning electron microscope (SEM) (Model Quanta 650 FEG) at different magnifications. The fracture surface was coated with a very thin layer of Pd/Pt material before performing SEM observations to prevent charging of the specimens from the electron beam. Figures 9 and 10 show the detailed fractography of the H-100 and glass specimens, respectively. The fracture surfaces of these materials exhibit many similar features at the early state of the crack growth. First, it appears that initiation of the crack occurred on the pre-crack front very close to the transition point identified through the analysis presented in Sect. 3.2. The fact that nucleation occurs at the transition point is not

surprising; either fracture criterion under consideration would indicate such initiation. The key difference is in the prediction of the onset of fragmentation of the crack front. Second, the fragmentation of the crack front into multiple facets is immediate! This is clearly observed by noting that in the neighborhood of the transition point there does not exist a flat area where pre-crack front grows without fragmentation. For the glass specimen, if the threshold twist angle of 3.3° indicated by Sommer (1969) is to hold, a straight extension of the crack front is expected over a length of about 2.044 mm, but it is seen that fragments appear within the distance of 100 μm from the transition point. Within this distance the value of $K_{III}^{\infty}/K_{I}^{\infty}$ is only marginally different from zero. The same behavior is also observed in Fig. 9 in H-100, with immediate fragmentation of the crack over a length that is nearly the same as in the glass specimen. Taken together, these observations suggest that there appears to be no threshold value of $K_{III}^{\infty}/K_{I}^{\infty}$ required for fragmentation of the crack front; a crack front will fragment immediately as soon as it is perturbed by mode III. It remains to identify the scale on which such fragmentation is observed and we will consider some aspects of this problem in the next section. Finally, beyond the initiation of crack growth at the transition point, further crack growth occurred dynamically, dominated by mode I loading. This specimen design was not suitable for examining continued crack growth, if any, under the combined mode loading

Fig. 10 **a** Fractograph of glass specimen type I, showing the region near the transition point. (*a1*) Shows a magnification of the boxed region in **a**; (*a2*) Shows a magnification of the boxed region in **a1**. **b** Identifies the region of interest (near the transition point) where there is a transition from positive K_{III}^{∞} to negative K_{III}^{∞}
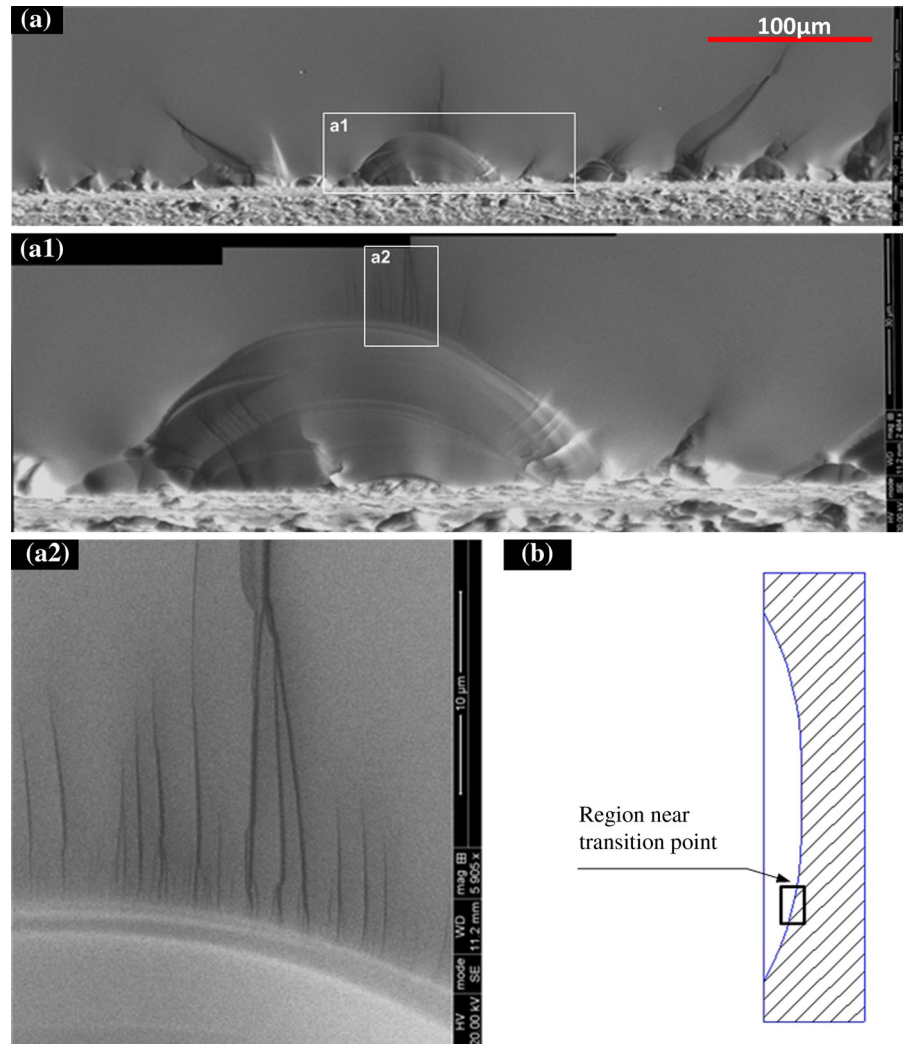
4.2 Intrinsic length scale

While the specimen Type I was well suited for considering the possible threshold behavior, continued growth was dominated as indicated above by mode I. Therefore, experiments were performed on H-100 with specimen Type II, where it was anticipated that as a result of the negative K_I^{∞}, the nucleated fragments along the crack front may get arrested. However, cracks initiated along the region of the positive K_I^{∞} on the pre-crack front (see Fig. 7, between 0.9 and 1.0 *s*), grew faster than the cracks nucleated in other regions, and quickly reached an unstable state, popping across the entire specimen dynamically. Nevertheless, the unstable cracks deviated away from the machined crack fronts, and left parts of specimen containing "unbro-

ken" portions of the pre-crack that could be examined to evaluate the nucleation of fragments from the machined pre-crack. These unbroken portions were recovered, polished to extremely thin sections on planes above and below the pre-crack surface and imaged by an optical microscope with magnification of $100\times$, $200\times$ and $300\times$; these images are shown in Fig. 11. It is worth emphasizing that fragmentation spacing can be observed at three different length scales in these specimens. The third level, the largest scale observed, is shown in Fig. 11a. The pre-crack front is identified by an arrow; the width of the crack is dictated by the blade used to cut the crack and as indicated earlier, this is on the order of 175–200 μm. At this level, the nucleated cracks are easily observed, and are indicated in Fig. 11a, b; they appear to form a nice nearly periodic

Fig. 11 Cascading length scales of fragmentation spacing. **a** Nucleation along the pre-crack front on the scale of the thickness of the machined crack. A high magnification image covering a longer length along the crack front is provided as Supplementary Material. **b** Nucleation along the pre-crack front influenced by the width of the *groove lines* in the machined crack. **c** Nucleation along a natural crack front. (*d*) A magnified view of the boxed region (100 μm × 500 μm) indicated in **c**
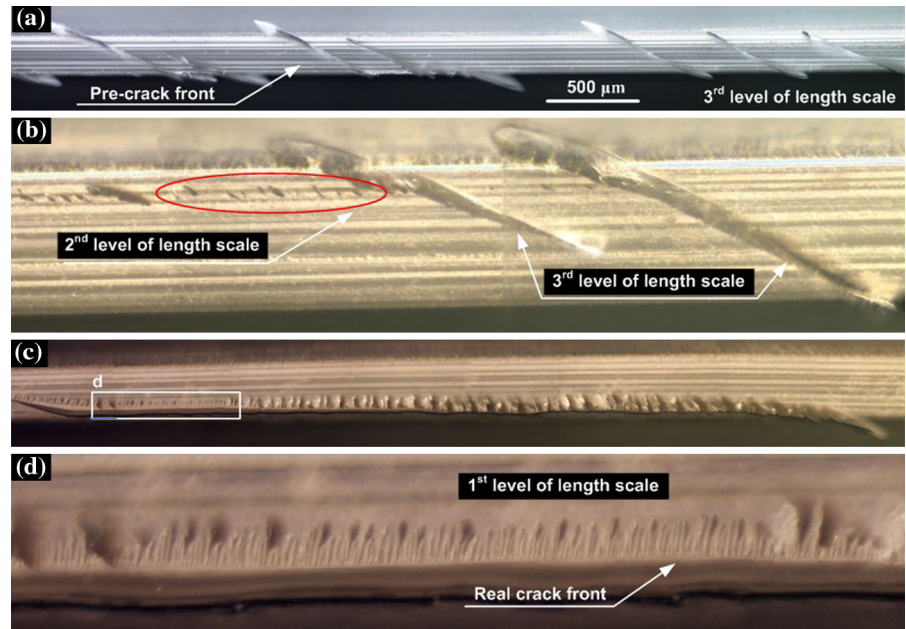
pattern with a spacing of about two pre-crack thicknesses, but also indicate significant fluctuations. There exists a smaller length scale—the second level—that is associated with the width of the groove lines on the pre-crack front. As indicated earlier, in addition to the thickness of the blade that dictates the thickness of the pre-crack, the crack front is decorated with grooves that arise from the size of the cutting particles that are part of the cutting blade. These grooves are on the order of a few tens of microns in size and run along the entire crack front. Nucleation of fragments that occur at these grooves results in fragments with a spacing of a few tens of microns. Finally, fragmentation at the smallest length scale—the first level—was discovered along natural crack front (Fig. 11c, d). The thickness of a naturally formed crack is typically much smaller than the machined cracks and is of the order of the fracture process zone. Therefore, one expects the lower bound of the fragment spacing to be dictated by this microstructural scale, as indicated by the results of Lin et al. (2010). Indeed, fragments that were nucleated from a natural crack exhibited a much smaller fragmentation spacing in comparison to the machined cracks; optical microscopy resolved this spacing to be about 10 μm, but there could be much smaller features that are not resolved optically.

The SEM images for glass specimen discussed in Sect. 4.1 (Fig. 10a2) also manifest the cascading length scale of fragment spacing. The larger spacing in Fig. 10a is associated with the width of the machined pre-crack. But in Fig. 10a2 a small region along the natural crack front captured at extremely high magnification is shown. It is worth emphasizing that the fragmentation spacing of a natural crack front is of the order of 0.5–1.0 μm which is much smaller than the fragmentation spacing for the machined crack front for glass.

For the specimens used in Sect. 4.1, over the distance of 100 μm near the transition point, the ratio of $K_{III}^{\infty}/K_I^{\infty}$ is nearly the same for both the glass and H-100 specimens ($K_{III}^{\infty}/K_I^{\infty} \sim 0.001$). Based on the dependence of the fragmentation spacing on the fracture process zone predicted by the stability analysis of Pons and Karma (2010) (Eq. 4) one would expect differences between glass and H-100, because the fracture process zone size in H-100 is about two orders of magnitude larger than that of glass. But it can be observed clearly that the fragmentation spacing is approximately of the order 30 μm for both materials (see Figs. 9, 10).

Together, these observations indicate that an intrinsic length scale for the crack front fragmentation spacing does not exist, but that the spacing depends on the characteristic dimension of the driving crack (thickness of the crack). This provides an explanation for the fact that fragmentation of the crack front has been observed in scales ranging from the microscale to the geological scale where the fragmentation space may

be on the order of meters. In the following, we will explore the effect of the stress field shielding from one nucleated crack front on the neighborhood of this nucleus.

4.3 Shielding along the crack front resulting from nucleation of a fragment

As discussed in Sects. 1 and 2, there have been many attempts at understanding the initiation of cracks under mixed mode I+III. Almost without exception, these investigations have used the approach of getting the stress intensity factor using a perturbation approach in which a continuous (smooth) evolution from the "parent" crack was considered. Linear stability analysis was then considered on the basis of the PLS criterion; as discussed earlier, the predictions of such analysis, for example by Leblond et al. (2011), indicate that the crack path is stable for much larger values of $K_{III}^\infty/K_I^\infty$ than observed experimentally. However, if the PLS generalization in Eq. (6) is used, we expect crack front to fragment into multiple cracks; we explore the possible origins of the fragment spacing under this criterion through a series of numerical simulations. In order to explore the changes in the SIF that is triggered by the nucleation of crack front fragments, we introduce a fragmented crack in the middle of the parent crack; we shall call this the "daughter" crack. Because of limitations in the BEM code in representing intersecting cracks, the following strategy was adopted. The parent crack was represented as a sharp crack in a large block of size $(a \times b \times c)$. The specimen was subjected to boundary loading that generated a mixed mode loading $\left(K_I^\infty, K_{III}^\infty\right)$ along the straight crack front. The daughter crack was represented by a three-dimensional geometrical feature: the daughter crack was idealized as a disk-like geometrical feature with a "crack tip radius" $r_{\text{micro}} = 12.7$ μm, with a circular crack of radius $a_{\text{micro}} = \alpha r_{\text{micro}}$, and $\alpha \in [5, 50]$. The nucleated crack was taken to be orientated at an angle ϕ_c, as dictated by Eq. (2). The system of the parent-daughter cracks is shown in Fig. 12a. The variation of the stress intensity factors (k_I, k_{II}, k_{III}) along the original crack front that results from nucleation of the daughter crack was calculated from the boundary element simulation. This variation is shown in Fig. 12b, where the stress intensity factors are normalized by K_I^∞ and the distance along the crack front from the daughter crack is normalized by

the radius of the daughter crack. The results shown correspond to $K_{III}^\infty/K_I^\infty = 0.42$, resulting in $\phi_c = 35°$, and for $\alpha \in [5, 50]$, corresponding to a daughter crack of radius $a \in [63.5, 635]$ μm. The shielding effect of the nucleated crack on either side of the daughter crack is evident: the stress intensity factors for modes I and III on the parent crack drop in the immediate vicinity of the microcrack; with distance away from the site of the daughter crack, the stress intensity factors along the parent crack gradually return to the far-field values that correspond to the imposed uniform values, with a small peak at about one radius from the daughter crack. A local fluctuation in the mode II stress intensity factor is also introduced, indicating the inherent coupling of all three modes. It is clear that any crack nucleation that occurs along the crack front will shield—by elastic unloading—a neighborhood whose size depends on ϕ_c and α. In order to obtain a quantitative measure of this shielding, we need to identify the location at which the next crack may nucleate: this could be at the site of maximum k_I located at a distance b_1 from the nucleation point. However, there is a significant amount of k_{III} at this location; nucleation could also occur at the location of minimum k_{III}, which is located at a distance b_3 from the nucleation point. The distances b_1 and b_3 could be considered to indicate the spacing between the nucleated cracks corresponding to any twist angle ϕ_c and crack size α. These simulations were repeated for values of $\phi_c \in [10, 35]$ at fixed $\alpha = 20$ and the results of mode I and III stress intensity factors, $\left(k_I/K_I^\infty, k_{III}/K_{III}^\infty\right)$ were obtained. From these results, the dependence of the distances b_1 and b_3 on ϕ_c were extracted and are plotted in Fig. 13. From these results, it is seen that b_1 increases with ϕ_c while b_3 indicates a decrease with an increase in ϕ_c; the latter trend is similar to that indicated in the experimental results of Lin et al. (2010) (see Fig. 7c of that reference). The implication of this result is that the shielded length (and therefore the fragment spacing) depends on the size of the daughter crack, which in turn, would depend on the characteristic thickness of the parent crack that drives the nucleation. We conclude this discussion by pointing out that we have only considered the nucleation of the crack fragments and not its further evolution. Upon further loading, the nucleated population of daughter cracks will interact with each other, and create a quite complex state of local mode mix. The further evolution of the daughter cracks follows one of two possible paths: if the global loading is dominant K_I^∞, the daugh-

Fig. 12 **a** Schematic diagram indicating the parent crack under a mixed mode loading, with a daughter crack that nucleated at the center. **b** Change in crack tip SIFs with daughter cracks size $a_{micro} = \alpha r_{micro}$. The daughter crack tip was idealized by a rounded geometrical feature $r_{micro} = 12.7\,\mu m$ in the simulations. The parent crack is loaded such that $K_{III}^{\infty}/K_{I}^{\infty} = 0.42$ (to produce the twist angle $\phi = 35°$). The distance along the parent crack front from the daughter crack is normalized by a_{micro}

(a)

(b)
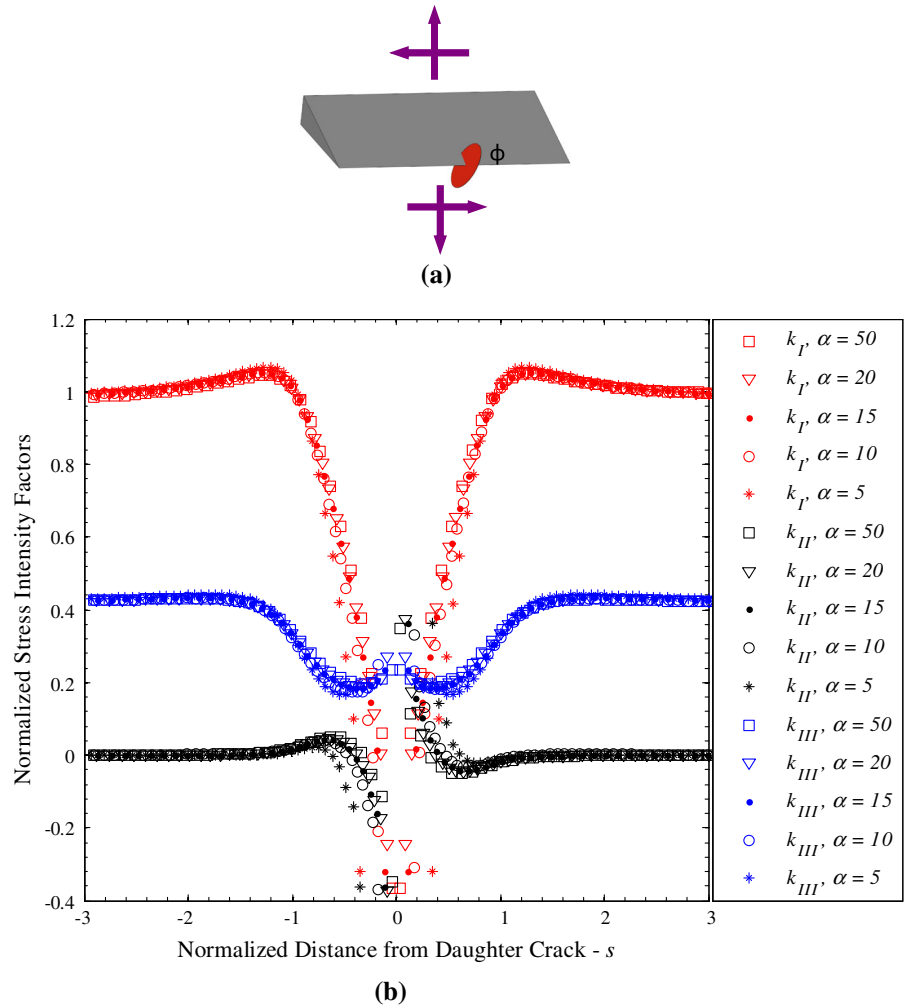
ter cracks will eventually coalesce into each other and rotate the crack so as to eliminate K_{III}^{∞}. On the other hand, if the global loading is dominant K_{III}^{∞}, within a compressive field (negative K_{I}^{∞}), the fragments may continue to grow as independent cracks as indicated in the experiments of Goldstein and Osipenko (2012) and in the type II specimens reported in the present work.

5 Conclusion

The criterion for initiation of cracks under mixed-mode I+III loading has been examined further. Following on the geometry suggested for such investigations by Goldstein and Osipenko (2012), we explored alternative geometries that can be tailored to address spe-
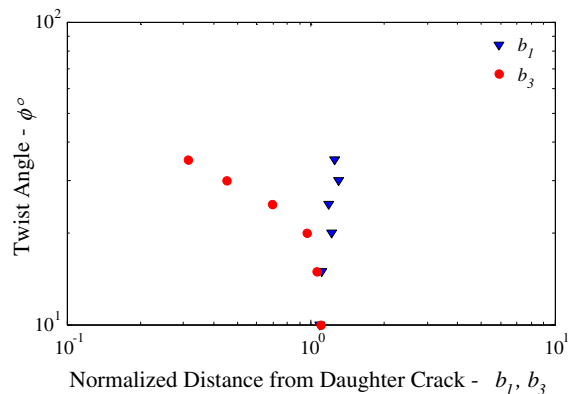

Fig. 13 Location b_1 of maximum k_I and b_3 of minimum k_{III} for different daughter cracks angles ϕ. The daughter crack tip was idealized by a rounded geometrical feature $r_{micro} = 12.7\,\mu m$, with crack size $a_{micro} = \alpha r_{micro}$; $\alpha = 20$ in these simulations

cific questions related to the initiation of cracks. All designs were supported with calculation of the stress intensity factors using a boundary element code (Li et al. 1998). With the first design, mode II was nearly completely eliminated, and the value of the mode III stress intensity factor experienced a change of sign from negative to positive in the location where the mode I stress intensity factor attained a maximum. This allowed examination of the question of existence of a threshold for crack front fragmentation. The second design, in which the mode I stress intensity factor was negative caused crack that nucleated to be arrested, permitting examination of the spacing between the nucleated crack front fragments. Experiments were performed on two materials: glass and H-100, both of which exhibit brittle or quasi-brittle fracture behavior. Recovered specimens were examined to reveal the geometry of the nucleated crack front fragments. From this study, two major conclusions are reached:

i. Cracks subjected to combined modes I+III loading cause fragmentation of the crack front *without any threshold*; perturbations as small as $K_{III}^{\infty}/K_I^{\infty} \sim$ 0.001 cause nucleation of fragmented daughter cracks.
ii. The distance between the fragments is dictated by the length scale corresponding to the decay of the elastic field; this decay depends on the thickness dimension of the parent crack from which the daughter fragments are nucleated. The thickness of the parent crack is governed either by the microstructural scale of the fracture process zone for a natural crack, or by the local radius of curvature of grooves for a machined crack.

The continued growth or coalescence of the nucleated crack fragments, which themselves could be subjected to further mixed mode loading, would depend on the global loading imposed and will been examined in a future contribution.

6 Appendix: Tables of stress intensity factors for part-through cracks for specimen types I, II and III

The variation of the stress intensity factor along the crack front for the original Goldstein–Osipenko geometry and its variants used in this work, labeled Type I, II and III specimens are provided here; the stress intensity factors were calculated using a boundary element code developed by Li et al. (1998).

See Tables 1, 2 and Fig. 14.

**Table 1** Stress intensity factors for Goldstein–Opisenko configurations

s	K_I^{∞}	K_{II}^{∞}	K_{III}^{∞}	s	K_I^{∞}	K_{II}^{∞}	K_{III}^{∞}
0.000	0.031	0.100	0.052	0.533	−0.200	0.003	0.341
0.022	−0.036	0.034	0.060	0.594	−0.177	0.000	0.334
0.047	−0.076	0.021	0.069	0.650	−0.153	−0.003	0.324
0.074	−0.114	0.015	0.082	0.701	−0.124	−0.006	0.313
0.103	−0.153	0.013	0.101	0.748	−0.088	−0.009	0.299
0.136	−0.191	0.014	0.128	0.790	−0.042	−0.013	0.281
0.171	−0.226	0.015	0.163	0.829	0.017	−0.018	0.260
0.210	−0.252	0.017	0.204	0.864	0.089	−0.024	0.239
0.252	−0.267	0.017	0.247	0.897	0.172	−0.033	0.221
0.299	−0.269	0.016	0.286	0.926	0.260	−0.046	0.207
0.350	−0.260	0.013	0.317	0.953	0.347	−0.067	0.199
0.406	−0.243	0.010	0.336	0.978	0.429	−0.104	0.195
0.467	−0.223	0.006	0.344	1.000	0.492	−0.295	0.210

Table 2 Stress intensity factors for part-through cracks for types I, II and III

s	Specimen type I			Specimen type II			Specimen type III		
	K_I^∞	K_{II}^∞	K_{III}^∞	K_I^∞	K_{II}^∞	K_{III}^∞	K_I^∞	K_{II}^∞	K_{III}^∞
0.000	−0.003	−0.010	−0.022	0.000	0.000	0.000	0.001	−0.001	0.002
0.028	0.002	−0.054	−0.100	−0.039	−0.003	0.006	−0.029	−0.006	0.012
0.058	0.014	−0.055	−0.107	−0.058	−0.005	0.011	−0.047	−0.008	0.016
0.091	0.029	−0.048	−0.105	−0.075	−0.007	0.016	−0.065	−0.009	0.020
0.126	0.046	−0.040	−0.100	−0.091	−0.009	0.021	−0.083	−0.011	0.025
0.164	0.064	−0.031	−0.095	−0.106	−0.011	0.029	−0.101	−0.012	0.031
0.204	0.084	−0.024	−0.090	−0.120	−0.013	0.037	−0.117	−0.012	0.038
0.248	0.104	−0.017	−0.085	−0.131	−0.013	0.046	−0.132	−0.012	0.045
0.294	0.125	−0.010	−0.080	−0.139	−0.012	0.056	−0.145	−0.010	0.053
0.345	0.147	−0.004	−0.076	−0.144	−0.008	0.067	−0.155	−0.007	0.061
0.399	0.174	0.002	−0.074	−0.146	−0.002	0.077	−0.163	−0.001	0.069
0.450	0.199	0.002	−0.070	−0.144	−0.001	0.084	−0.167	0.000	0.074
0.500	0.221	0.002	−0.066	−0.136	−0.001	0.088	−0.166	0.001	0.076
0.550	0.239	0.003	−0.059	−0.125	0.000	0.089	−0.160	0.001	0.074
0.601	0.251	0.003	−0.051	−0.110	0.001	0.086	−0.150	0.002	0.069
0.655	0.261	0.007	−0.040	−0.092	0.008	0.081	−0.137	0.007	0.062
0.706	0.271	0.008	−0.030	−0.074	0.013	0.075	−0.125	0.010	0.054
0.752	0.277	0.008	−0.019	−0.057	0.016	0.069	−0.111	0.012	0.047
0.796	0.281	0.006	−0.009	−0.039	0.019	0.063	−0.096	0.013	0.040
0.836	0.280	0.003	0.001	−0.021	0.020	0.058	−0.080	0.012	0.035
0.874	0.275	0.000	0.010	−0.004	0.021	0.054	−0.063	0.012	0.030
0.909	0.265	−0.004	0.017	0.010	0.021	0.049	−0.047	0.011	0.026
0.942	0.247	−0.007	0.022	0.022	0.021	0.044	−0.031	0.010	0.022
0.972	0.211	−0.009	0.023	0.028	0.018	0.036	−0.016	0.009	0.017
1.000	0.023	−0.003	0.005	0.006	0.003	0.006	0.002	0.001	0.003

Specimen dimensions are indicated in Sect. 3.2 (with thickness $D = 0.5$). Poisson's ratio $\nu = 0.35$ and unit load distributed over the length of 0.38 for specimen type I and 1.0 for specimen types II and III have been assumed in the simulations

Fig. 14 **a** Mesh discretization of Goldstein–Osipenko configurations. **b** Typical mesh discretization for part-through crack configurations
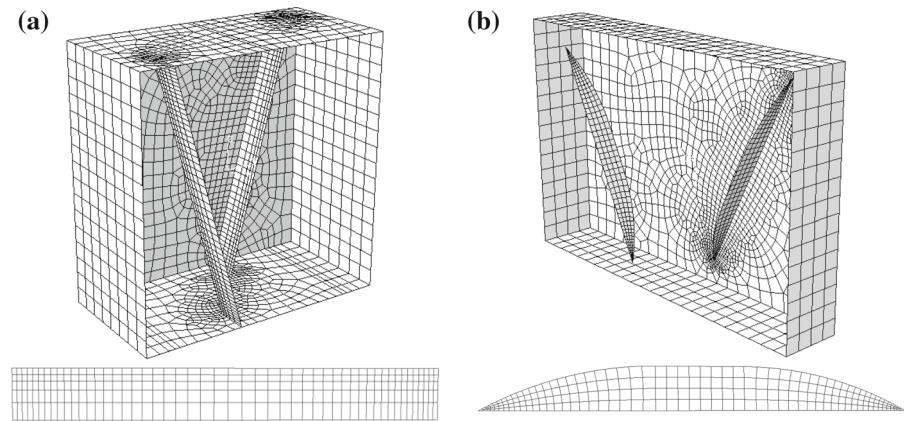
References

Barenblatt GI, Cherepanov GP (1961) On brittle cracks under longitudinal shear. Prikl Mech Math 25:1110–1119

Cooke ML, Pollard DD (1996) Fracture propagation paths under mixed mode loading within rectangular blocks of polymethylmethacrylate. J Geophys Res 101:3387–3400

Goldstein RV, Salganik RL (1974) Brittle fracture of solids with arbitrary cracks. Int J Fract 10:507–523

Goldstein RV, Osipenko NM (2012) Fracture structure near a longitudinal shear macrorupture. Mech Solids 47:505–516

Griffith AA (1920) The phenomena of rupture and flow in solids. Phil Trans Roy Soc Lond A221:163–198

Irwin GR (1957) Analysis of stresses and strains near the end of a crack traversing a plate. J Appl Mech 24:361–364

Knauss WG (1970) An observation of crack propagation in anti-plane shear. Int J Fract 6:183–187

Lazarus V, Buchholz F-G, Fulland M, Wiebesiek J (2008) Comparison of predictions by mode II or mode III criteria on crack front twisting in three or four point bending experiments. Int J Fract 153:141–151

Leblond JB (1999) Crack paths in three-dimensional elastic solids, I: two-term expansion of the stress intensity factors-application to crack path stability in hydraulic fracturing. Int J Solids Struct 36:79–103

Leblond JB, Karma A, Lazarus V (2011) Theoretical analysis of crack front instability in mode I+III. J Mech Phys Solids 59:1872–1887

Li S, Mear ME (1998) Singularity-reduced integral equations for displacement discontinuities in three-dimensional linear elastic media. Int J Fract 93:87–114

Li S, Mear ME, Xiao L (1998) Symmetric weak-form integral equation method for three dimensional fracture analysis. Comput Methods Appl Mech Eng 151:435–445

Lin B, Mear ME, Ravi-Chandar K (2010) Criterion for initiation of cracks under mixed-mode I+III loading. Int J Fract 165:175–188

Movchan AB, Gao H, Willis JR (1998) On perturbations of plane cracks. Int J Solids Struct 35:3419–3453

Pons AJ, Karma A (2010) Helical crack-front instability in mixed-mode fracture. Nat Let 464:85–89

Smekal A (1953) Zum Bruchvogang bei sprodem Stoffrerhalten unter ein und mehrachsiegen Beanspringen. Osterr Ing Arch 7:49–70

Sommer E (1969) Formation of fracture 'lances' in glass. Eng Fract Mech 1:539–546

Williams ML (1952) Stress singularities resulting from various boundary conditions in angular corners of plates in extension. J App Mech 19:526–528

Yates JR, Miller KJ (1989) Mixed-mode (I–III) fatigue thresholds in a forging steel. Fatigue Fract Eng Mater Struct 12:259–270